Analysis of Urban Heat Island Effect Based on Changes of Urban Surface Parameters

Xiufu Teng[1.2*], Kim Ji Eun[1]
[1]Graduate School of Techno Design, Kookmin University, Seoul, 136702, South Korea
[2]Academy of Art and Design, Yancheng Teachers University, Yancheng, 224007, China
astronautm@163.com

Abstract: With the accelerated development of urbanization and industrialization, the scope of cities continues to expand. However, natural landscape such as vegetation and water in the city has been transformed into artificial impervious water. This has aggravated urban heat island effect and caused serious damage to the urban ecological environment. To explore the relevant factors that affect urban heat island effect, this study selects Tianjin, which has a high level of urbanization and a significant heat island effect, as the study area. And land satellite remote sensing images from 2013, 2018, and 2022 were selected for data acquisition. The analysis was conducted from the perspective of urban surface parameters changes. The selected urban surface parameters for this study include vegetation index, water body index, impermeable surface index, and surface temperature index. The heat island area will increase over time. And in 2013, 2018, and 2022, the proportion of this area to the total area was 41.92%, 48.73%, and 49.16%, respectively. In 2022, the proportion of different regions in total area ranges from 40.21% to 54.22%. At this time, the heat island area of Dongli District is the largest and that of Jinnan District is the smallest. Surface temperature is negatively correlated with vegetation and water bodies, and positively correlated with impermeable water surfaces. Between 2013 and 2022, over 90% of impermeable water surfaces belonged to heat island area, over 80% of vegetation belonged to green island area, and over 97% of water bodies belonged to green island area. In conclusion, the method proposed in the study can well analyze urban heat island effect and urban surface parameters change's connection. This provides solid scientific data support for alleviating the heat island effect.

Keywords: Surface parameters; Heat island effect; City; Characteristics of spatiotemporal changes; Inversion; Relativity

Introduction

Global warming is more severe. This is due to greenhouse gases growth, such as carbon dioxide, which continuously increases the overall earth temperature. This seriously affects the balance of natural ecosystems and the safety of human survival [1-2]. In the context of global warming and sustainable development, urban heat island effect (UHIE) plays an important role in promoting green development in cities. UHIE is a phenomenon where urban areas with higher temperatures are surrounded or partially surrounded by suburbs with lower temperatures, through the combined action of multiple factors [3-4]. The process of urbanization and industrialization has contributed to UHIE enhancement [5]. UHIE also creates opportunities for the development of building energy-saving technology. The demand for building energy-saving technology is constantly increasing, and technologies such as solar energy utilization, ventilation systems, and green roofs are widely used in buildings, reducing energy consumption and environmental burden, while also addressing issues of high energy consumption and carbon emissions. However, UHIE has a great impact on mid to low dimensional summer areas. Continuous high temperatures can cause negative emotions such as irritability among residents living in the central area of the heat

island (HI) for a long time, and can also cause physical damage such as gastrointestinal diseases. In severe cases, it can also endanger people's life safety [6-7]. To prevent and manage UHIE, the study selected Tianjin as the research area, and sought targeted strategies to alleviate UEID through the selection and analysis of urban surface parameter (SP).

The research aims to seek solutions to alleviate UEID, reduce the level and intensity of urban heat, reduce air pollution caused by UHIE, and thus improve the living environment of residents. It also has a certain degree of practical significance for the long-term healthy development of the city in the future, the construction of Sustainable city and green development. The innovation points of the research mainly include the following two aspects. On the one hand, the principles of ecological landscape are applied to analyze the spatiotemporal changes in landscape patterns at the UHIE type level and landscape level. On the other hand, the relationship between urban SP index and urban heat island (UHI) is analyzed at multiple scales. The structure of the study mainly includes four parts. The first is a review of relevant research results. Secondly, it introduces the research area, the acquisition and treatment of urban SP, and the classification of UHI. Then, the spatial and temporal change characteristics of UHIE, the change analysis of SP and the correlation analysis of UHI and SP in the study area are analyzed using the method proposed in this study. Finally, there is a summary of this research.

1 Related Works

The advanced technology development has continuously optimized UHIE research methods. At present, there are remote sensing inversion method, meteorological observation method and boundary layer numerical simulation model method. These methods can be used not only individually, but also in combination with different methods. Numerous scholars have conducted in-depth research and exploration on this topic. Z. Li et al. combined remote sensing and measured data to address two serious issues of air pollution and UHIE in cities, and utilized a coupled coordination model. Taking Beijing as the research object, the spatiotemporal heterogeneity (SH) characteristics of interaction between PM2.5 and HI Effect (HIE) were studied. These measured results confirm that the relationship between PM2.5 and UHIE exhibits SH. The high coupling coordination zone of four seasons occurs above four seasons, covering an area exceeding 58.3% of Beijing's total area [8]. C. D. Tranaltes et al. conducted experiments on similar animals to investigate the impact of UHIE on animal behavior. If the UHIE induced sibiricide promotes a litter of animal cubs' survival and growth, it can promote urban population growth in reality [9]. E. Marques et al. found that UHIE has become a major health issue affecting the thermal comfort of urban residents. A thermometer embedded in daily private cars was studied to measure temperature. To evaluate the quality of this opportunistic data, this study provided local scale reference through two meteorological station networks in the cities of Dijon and Rennes in France, and tested the cooling effects of Rennes and Paris urban parks. Through research methods, each interested city in Western Europe can obtain similar maps to target key areas and support urban planning decisions [10]. R. Senguptaz et al. conducted a study to determine whether UHIE exists in Montreal, Canada, by obtaining temperature data through on-site sensors and government weather stations. Then they conducted correlation tests on temperature, demographic, and socio-economic variables. The results of regression testing show that they have no significant correlation due to spatial heterogeneity [11].

With UHIE research deepening, many researchers have shifted from studying the spatiotemporal distribution of UHI features to analyzing factors related to UHIE, to provide solid

scientific basis and methods for the alleviation of UHI. S. Mamatha et al. recorded different levels of fluoride in groundwater, tap water and lake water from 130 samples collected from different sources in Mysore area. Fluoride is a parameter for water quality analysis, which is non-degradable, and continues to exist in the environment. This study aimed to judge UHIE situation through water quality analysis [12]. M. A. Alatorre-Zamora et al. reported a study on basement fracture system of Matalan urban garbage dump in Guadalajara. And they conducted experiments through outcrop measurement and statistical analysis of magnetic lineation orientation. There is a good to general correlation between the measured fracture direction and linear elements characterized by gravity and magnetic anomalies. The horizontal derivative and dip angle describe the horizontal boundary of abnormal body. The micromagnetic method result is consistent with the fault direction and boundary established by edge detection technology. Lineament established by gravity and magnetic Euler Deconvolution is also consistent [13]. P. Salinas et al. found that exposure of animals to wood smoke pollution can have an impact on their offspring's morphology. Through histological, stereological analysis, and microscopic observation, this study found that the absence of mother's body exposed to wood smoke pollution can affect offspring's lung morphology, while air pollution and UHIE can seriously affect health [14]. G. Duan et al. found that the aerodynamic parameters of surface roughness and zero plane displacement height would have a crucial impact on Monin Obukhov similarity theory accuracy. The study created a large number of samples for aerodynamic parameters and morphology through random forest algorithm combined with nonlinear least square regression of log layer wind profile. The feature importance score can be used to identify the factors that affect surface aerodynamic characteristics, which may enlighten UHIE [15].

In summary, there are currently many studies on UHIE and related parameters' feature analysis. But there is limited literature on the relationship between UHIE and urban SP. To expand the analysis of UHIE and urban SP, the study takes Tianjin area as the research area. Remote sensing images (RSIs) from different time periods were selected for UHIE spatiotemporal feature change analysis, landscape pattern change analysis, urban SP analysis, and the relationship between UHIE and urban SP.

2 Research Methods

This chapter analyzes the subsequent UHIE and urban SP, with Tianjin as the research area. Urban SP is selected as vegetation index, water body index, impermeable surface index, and surface temperature index. Finally, different UHI levels are divided.

2.1 Research Area

In recent years, urbanization process has developed rapidly, and the land area of cities has been continuously expanding. Natural landscape around the city has also been transformed into an artificial opaque water surface, destroying its ecological environment. This also exacerbates city's HIE and further threatens city's ecological environment and energy use. Tianjin is one of five major central cities in China and the largest coastal open city in northern China, with significant UHIE [16-17]. Therefore, the study takes it as the research area to analyze city's HIE based on urban SP changes, providing a solid foundation for governance and mitigation of HIs. Figure 1 is a schematic diagram of the study area.

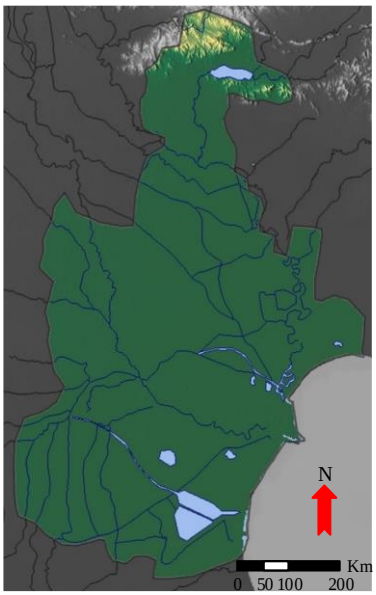

Fig.1 Schematic diagram of the research area

The study area is located on the west coast of the Pacific Ocean, in the northeast of North China Plain, bordering the Bohai Sea in the east, Yanshan Mountain in the north, and Beijing in the west. It is located at 38°34′~40°15′ N and 116°43′~118°43′ E. As of 2021, Tianjin has a total of 16 jurisdictions. The outer suburbs include Wuqing District and Baodi District. The central urban area includes Hebei District, Hexi District, Heping District, Hedong District and Hongqiao District. The environmental zone includes Dongli District, Xiqing District, Jinnan District and Beichen District, Jixian County, Jinghai County, Ninghe County and Binhai, covering an area of 119460 square kilometre [18]. As of 2022, there are 13.63 million permanent residents. The structural ratio of the first, second and tertiary sector of economy is 1.5:34.1:64.4. The geological structure of the study area is complex, with most of it covered by Cenozoic sediments. The terrain is mainly composed of plains and depressions, and the overall contour of the landform is high in the northwest and low in the southeast. The research area is mainly dominated by strong and smooth winds, belonging to the region where East Asian monsoon is prevalent, with a warm temperate semi humid monsoon climate. The main climatic characteristics are four distinct seasons, windy spring, drought and little rain, hot summer with concentrated rainfall, consistent cold and warm autumn, and cold and dry winter with little snow. The average annual precipitation in the study area ranges from 360mm to 970mm, and it spans both banks of Haihe River. The main stream has a total length of 71km, an average river width of 100m, and a water depth of 3-5m. In addition, there are 19 primary rivers flowing through the study area, with a total length of 284.1km. There are 79 secondary rivers with a total length of 1363.4km. There are 1061 deep canals with a total length of 4578km. Finally, the study area belongs to non volcanic Sedimentary basin medium low temperature hot water geothermal, with water temperature of 30 ℃~90 ℃, which is characterized by shallow burial and good water quality. At present, the discovered geothermal origin area with exploration and development value is 2343 Square kilometre, and the total hot water storage is 110.36 billion cubic meters. According to current research on Tianjin's HI, the HI area rapidly radiates outward from the central urban area. The UHI benefits of the central urban area, the four districts around the city and Binhai show a trend of connecting into pieces. Therefore, the central urban area and surrounding area were selected as typical research

areas for the study.

2.2 Data Acquisition and Preprocessing

As the social process of Tianjin continues to advance, the population has significantly increased. Vegetation, water bodies, and impervious surfaces have undergone significant changes in ground cover types, and temperatures have also shown a long-term trend of sustained growth [19-20]. Therefore, the research period is from 2013 to 2022. In addition, due to the time interval between obtaining data images and atmospheric environment impact, three time points were ultimately selected: August 30, 2013, July 23, 2018, and August 25, 2022. The images taken during this period are all without special weather interference, and can be used for studying the spatiotemporal variation characteristics of UHI and urban SP with an interval of 3-5 years. Landsat (LS) series of satellites have a large amount of data and a long time, making it easy to obtain. And to avoid differences in satellites processing, LS remote sensing data selected in this study was downloaded through Geospatial Data Cloud Platform. It has a good impact on imaging quality and can be used for subsequent result analysis. Table 1 shows the specific information of remote sensing data sources.

Table 1 Specific information of remote sensing data sources

Image time		2013-8-30	2018-07-23	2022-08-25
Satellite type		LS-7	LS-8	LS-8
Sensor type		ETM+	OLI_TIRS	OLI_TIRS
Track number		122-33	122-33	122-33
Spatial resolution	PAN	15	15	15
	REF	30	30	30
	THM	60	30	30

The specific information of LS series satellite bands is as follows: blue band is used to distinguish soil and vegetation. Red band is used to distinguish artificial ground objects. Green band is used to search for healthy green vegetation's reflectance. Near-infrared band is used to search for biomass. Mid infrared band is used to distinguish snow from clouds and determine water content. Thermal infrared band is used to invert surface temperature. Shortwave infrared band is used to classify rock types. Panchromatic band can fuse images and improve resolution. When obtaining ground information from satellites, errors may occur due to various factors, and geometric correction is necessary first. In the experiment, software ENVI5.3 was used to perform geometric correction on the RSIs of three time periods, ensuring that the errors were controlled within a reasonable range. After completing geometric correction, it is also necessary to resample the grayscale values of input image. The current effective resampling method is cubic convolutional interpolation method, which uniformly sets RSI's spatial resolution at each time period to 30m. Finally, Extract by Mask software in AreGIS was used to irregularly crop images from different time periods and extract the required RSI maps of research area.

2.3 Selection and Processing of Urban SP

UHIE is a phenomenon that occurs when a city reaches a certain scale and forms a high-temperature island. This is due to changes in the nature of urban underlying surfaces, air pollution, and the emission of artificial waste heat, which have significantly higher temperatures in cities than in suburbs. Therefore, changes in surface temperature were selected as urban SP. In addition, from the perspective of urban surface coverage, surface coverage types in the study area consists of preparation, water body and impervious surface. The vegetation mainly consists of

artificially cultivated green spaces, as well as crops and orchards in farmland. Water bodies mainly include rivers, lakes, and reservoirs, while impermeable surfaces include urban construction land, transportation facility land, and industrial land. According to previous research results, UHIE formation is closely related to vegetation, water bodies, and impermeable surfaces. Therefore, city SP selected for this study was surface temperature, vegetation, water body, and impermeable surface, and the corresponding SP index was selected for quantitative research. The vegetation parameter selection is Normalized Vegetation Index (NDVI), which has good detection performance for vegetation growth status and index coverage in equation (1).

$$NDVI = (NIR - \mathrm{Re}\,d)/(NIR + \mathrm{Re}\,d) \quad (1)$$

In equation (1), NIR and $\mathrm{Re}\,d$ refer to the near-infrared and red bands, respectively, $NDVI \in [-1,1]$. When $NDVI \in (0,1]$, it represents the presence of vegetation cover in this area. When $NDVI$ value is higher, vegetation coverage is better. Modified Normalized Water Body Index (MNWBI) is selected as water body index. Compared with other mainstream water body index methods, this method can clearly distinguish cities' water body information in RSIs. Equation (2) is the expression.

$$MNWBI = (Green - MIR1)/(Green + MIR1) \quad (2)$$

In equation (2), $Green$ and $MIR1$ represent green band and mid infrared band 1, respectively. The extraction methods of impermeable surface mainly include extracting through the negative correlation theory between impermeable surface and vegetation cover, and obtaining based on different spectral analysis models. Normalized Impervious Water Index (NIWI) is selected as the impermeable surface index in equation (3).

$$NIWI = \frac{TIR - \left[(MNWBI + NIR + MIR1)/3\right]}{TIR + \left[(MNWBI + NIR + MIR1)/3\right]} \quad (3)$$

In equation (3), TIR is a thermal infrared band that undergoes linear stretching from 0 to 255. $MNWBI$ is the corrected normalized water body index. $NIWI$ constructs an index through multiple bands such as thermal infrared and near-infrared to distinguish impermeable surfaces. Mono window algorithm (MWA) can make surface temperature retrieved. It is a relatively mature, simple and accurate surface temperature retrieval algorithm at present. It consists of surface specific radiance ψ, atmospheric transmittance ϑ and average atmospheric interaction temperature T_A in Formula (4).

$$\begin{cases} T_S = \left\{ d\square(1-R-S) + \left[g(1-R-S) + R + S \right] T_B - S T_d \right\} / R \\ R = \psi\vartheta \\ S = (1-\vartheta)\left[1 + (1-\psi)\vartheta \right] \end{cases} \quad (4)$$

In equation (4), T_S, T_B, and T_d are surface temperature, brightness temperature, and average atmospheric action temperature, respectively. d and g are both constants. T_B is the physical temperature of a blackbody when its radiance is equal to that of blackbody. It can convert

thermal infrared radiation brightness images into brightness temperature images through Planck equation. Equation (5) is the conversion formula.

$$LS(\alpha) = Gain \cdot DN + Bias \quad (5)$$

In formula (5), $LS(\alpha)$ represents the Radiant intensity received by the remote sensor. $Gain$ and $Bias$ are both gain and offset values, respectively. DN represents RSI pixel's brightness value. The expression for brightness temperature can be obtained from $LS(\alpha)$ in equation (6).

$$T_B = \frac{K_2}{\ln\left[1 + K_1 / LS(\alpha)\right]} \quad (6)$$

In equation (6), K_1 and K_2 are preset constants before satellite launch, which can be obtained from Table 2.

Table 2 LS series satellite thermal infrared band parameter information

Satellite	Sensor	*Gain*	*Bias*	$K_1 / \left(Mwcm^{-2}sr^{-1}\mu m^{-1}\right)$	K_2 / K
LS7	ETM+	0.037	3.200	666.090	1282.710
LS8	Brand10	3.3420×10^4	0.10000	774.890	1321.080
	Brand11			480.890	1201.140

In the LS8 remote sensing data, there are two thermal infrared bands Brand10 and Brand11, which correspond to 10.60-11.19 μm and 11.50-12.51 μm respectively. Brand10 is selected for inversion of Brightness temperature. ψ is estimated based on $NDVI$ and is determined by surface material composition and remote sensor's wavelength range. Equation (7) represents the relationship between different surface proportions and ψ.

$$\begin{cases} NDVI > 0.7, \psi = 0.99 \\ 0.05 \le NDVI \le 0.7, \psi = 0.004 P_{vn} + 0.986 \\ NDVI < 0.05, \psi = 0.973 \end{cases} \quad (7)$$

In equation (7), $NDVI > 0.7$, $0.05 \le NDVI \le 0.7$, and $NDVI < 0.05$ correspond to complete vegetation, mixed pixels, and completely bare soil. P_{vn} represents the proportion of vegetation composition in equation (8).

$$P_{vn} = \left(\frac{NDVI - NDVI_l}{NDVI_v - NDVI_l} \right)^2 \quad (8)$$

In equation (8), $NDVI_v$ and $NDVI_l$ are 0.7 and 0.05, respectively. ϑ is obtained through the atmospheric estimation equation of MWA algorithm, which has two types: high and low temperatures. Due to the acquisition of RSI in study area from July to August, a high temperature atmospheric profile was selected in equation (9).

$$\begin{cases} 0.4 \le \chi \le 1.6, \vartheta = 0.978429 - 0.080070\chi \\ 1.6 \le \chi \le 3.0, \vartheta = 1.031412 - 0.115360\chi \end{cases} \quad (9)$$

In equation (9), χ represents the moisture content. T_d is estimated using MWA algorithm. Due to the flight altitude of LS satellite being 725km, atmospheric moisture content can be set to 0. And after calculation, it can be concluded that under standard atmospheric conditions, T_d and the temperature near ground are linear functions. Linear function depends on atmospheric profile. By studying the geographical location and RSI of this region, atmospheric profile can be determined as the mid latitude summer average atmosphere. Equation (10) is the calculation of T_d.

$$T_d = 0.92621T_0 + 16.01100 \quad (10)$$

In equation (10), T_0 represents the near surface temperature, which can be obtained by the atmospheric temperature corresponding to time point from image. The temperature also needs to be converted to Kelvin (K).

2.4 Classification of UHI levels

There are three main methods for determining UHI through RSI. The first method is to divide T_B by mean standard deviation method or equal deviation method, with high temperatures being the HI area. The second method is to normalize T_B based on annual seasonal time differences, and then determine HI area according to method one. The third method is to divide the HI area based on surface temperature inversion using no less than 3 RSIs from different seasons of year, and select the shared high temperature as the HI area. Method one does not take into account the impact of seasonal changes, so partitioning accuracy will be affected. Method three is not suitable for relevant research on time series, and data amount and computation are very large. Based on the above UHI determination method, this study selected urban thermal field variation index for quantitative analysis of UHIE in equation (11).

$$UTFVI(T) = \frac{T_j - T_\mu}{T_\mu} \quad (11)$$

In equation (11), T_j stands for the surface temperature value of j-th pixel. T_μ refers to study area's average surface temperature. To more intuitively and clearly describe the spatiotemporal characteristics of UHIs, this research uses threshold method to classify. The specific UHIE grades are as follows. When $UTFVI(T)$ is>0.15, 0.10~0.15, 0.05~0.10, 0~0.05 and<0, the corresponding HI grades are very strong HI (VU), strong HI (QU), medium HI (MU), weak HI (RU) and green island (GU).

3 Analysis of UHIE and SP Changes

To analyze the changes in UHIE and urban SP, this study first analyzes UHIE spatiotemporal

characteristics. Secondly, UHIE landscape pattern was analyzed. Then, the changes in urban SP were analyzed. Finally, the correlation between UHI and urban SP was analyzed.

3.1 Analysis of Spatiotemporal Variation Characteristics of UHIE

When analyzing UHIE of study area, time distribution characteristics from 2013 to 2022 were first analyzed.

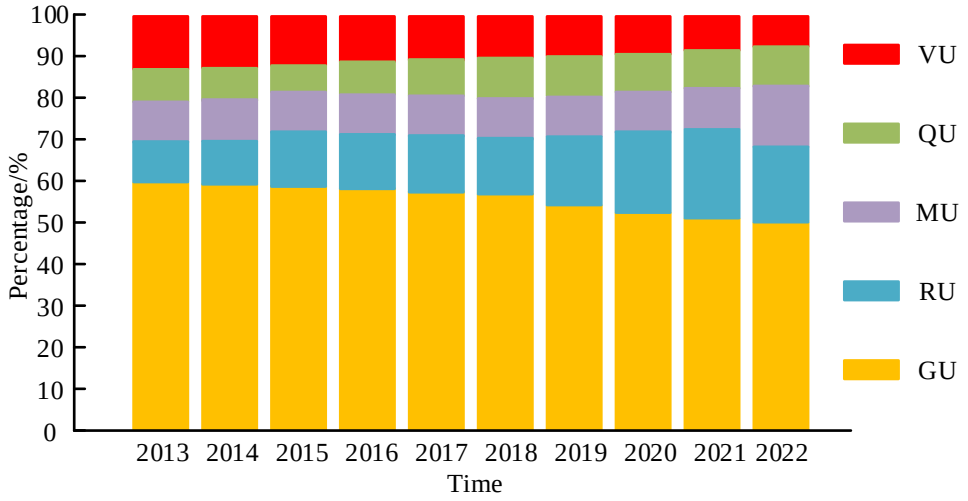

Fig.2 The distribution of HI levels at different time phases

Figure 2 shows HI grades distribution in different phases of the study area. In Figure 2, the increase in time leads to an increase in HI area. And in 2013, 2018, and 2022, the proportion of HI area to the total area was 41.92%, 48.73%, and 49.16%, respectively. The slowdown of HI area from 2018 to 2022 may be due to COVID-19, with most factories shut down and residents isolated at home. Therefore, the climate environment has been alleviated to a certain extent. The proportion of VU continues to decrease over time, from 6.95% in 2013 to 3.71%, and RU and MU overall show an increasing trend. Based on these results above, temporal distribution characteristics of HIs within the study area show a shift from being dominated by extreme HIs to being dominated by weak HIs. Then, the spatiotemporal characteristics area were analyzed.

Table 3 The distribution of HI area in different time periods and regions within the study area

Region		Time	RU	MU	QU	VU	HI area ratio
Downtown		2013	5.94	13.53	22.39	55.76	97.62
		2018	10.01	21.37	36.08	27.41	94.87
		2022	15.61	35.29	31.06	10.58	92.54
Four districts around the city	Dongli district	2013	12.58	8.28	5.18	7.91	33.95
		2018	15.81	11.52	9.15	11.41	47.89
		2022	20.57	15.77	9.12	8.76	54.22
	Xiqing district	2013	18.82	10.26	5.73	6.38	41.19
		2018	14.02	8.82	6.61	4.19	33.64
		2022	18.03	13.66	7.12	4.45	43.26
	Jinnan district	2013	15.12	8.69	5.12	6.17	35.10
		2018	14.79	11.86	6.12	5.39	38.16
		2022	16.92	11.86	6.07	5.36	40.21

Beichen district	2013	14.32	8.03	5.27	9.14	36.76
	2018	11.27	8.01	7.64	7.82	34.74
	2022	12.67	11.13	8.68	8.29	40.77

Table 3 shows the distribution of HI area in different time periods and regions within the study area. In Table 3, 97.92% of central urban area became a HI area, and showed a decreasing trend from 2018 to 2022. Among them, VU decreased more significantly, from 55.76% in 2013 to 10.58% in 2022, a decrease of 45.18%. The area of RU and MU has significantly increased, from 19.47% in 2013 to 50.90% in 2022, an increase of 31.43%. The HI area corresponding to fours around city shows an overall growth trend. In 2013, the proportion of different regions in total area ranged from 33.64% to 41.19%. Jinnan has the largest HI area and Xiqing is the smallest. In 2022, the proportion of different regions in total area ranges from 40.21% to 54.22%. At this time, the HI area of Dongli is the largest and Jinnan is the smallest. Both Xiqing and Beichen showed a trend of first decreasing and then increasing, while the HI area in Dongli continued to increase. However, there was a minimal downward trend in some HI levels in 2018. And the registered areas of different HIs are RU, MU, QU, and VU, from large to small. The HI area of Jinnan continued to increase from 2018 to 2022, mainly RU and MU. To further analyze the reasons for the spatiotemporal changes in UHIE, two typical regions were selected for observation in this study.

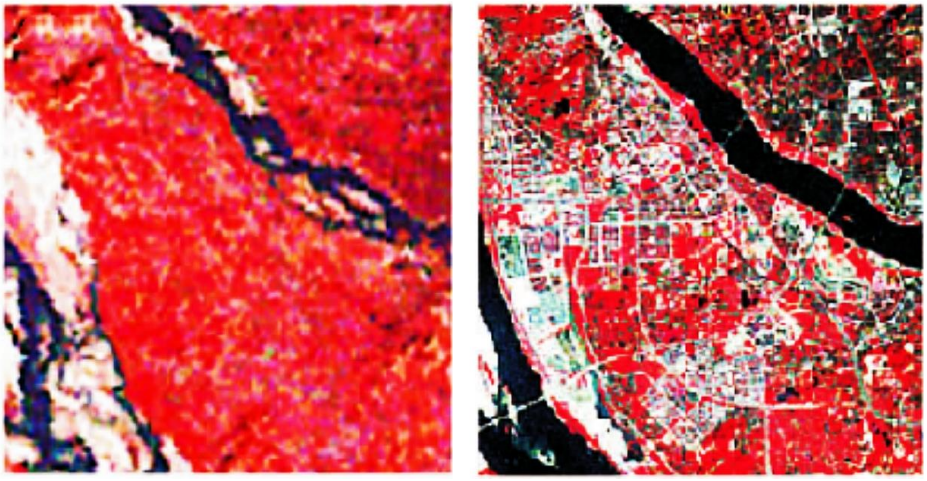

(a)Typical Region 1 in 2013 (b)Typical Region 1 in 2022

(c)Typical Region 2 in 2013 (d)Typical Region 2 in 2022

Fig.3 Typical area of Urban HI change

Figure 3 shows a comparison of typical areas of UHI changes, with the red part indicating vegetation coverage areas. Figure 3 (a) and Figure 3 (b) show the comparison of HI changes in typical region 1 in 2013 and 2022, respectively. In 2013, there was still a large area of farmland in typical area one. But in 2022, a large amount of farmland will be converted into construction land,

and HI area will also grow rapidly. Figures 3 (c) and 3 (d) show the comparison of HI changes in typical region 2 in 2013 and 2022, respectively, with the dark purple part representing the water body. The area at water body edge is transformed into construction land, and HIs are mainly distributed around the construction land, with no HI distribution near the water body.

3.2 UHIE Landscape Pattern Analysis

To analyze UHIE landscape pattern, this study is based on landscape ecology and calculates landscape index to analyze the evolution characteristics of UHIE's landscape pattern.

Table 4 Selection of UHIE Landscape Pattern Index

Type'	Landscape index	Type level index	Landscape level index
Number	Type area (TA)	TA	/
	Type proportion (TP)	TP	/
	Bambi number (NP)	NP	NP
	Patch density (PD)	PD	PD
	Maximum patch index (MPI)	MPI	/
Shape	Mean patch area (MPA)	MPA	MPA
	Area weighted shape index (ASI)	ASI	ASI
	Average proximity index (API)	API	/
	Degree of polymerization (DP)	/	DP
	Spread degree (SD)	/	SD
Structure	Dispersion and juxtaposition index (DJI)	/	DJI
	Diversity index (DI)	/	DI
	Evenness index (EI)	/	EI

Table 4 shows the selection content of UHIE landscape pattern index. In Table 4, the landscape pattern evolution characteristics of the study area at both type level and landscape level are represented by three features: data, shape, and structure. The landscape index is obtained through Fragstats software. MU and QU have a greater impact on residents in the study area. The changes of MU, QU and VU landscape indexes in the past ten years are observed from landscape pattern type level.

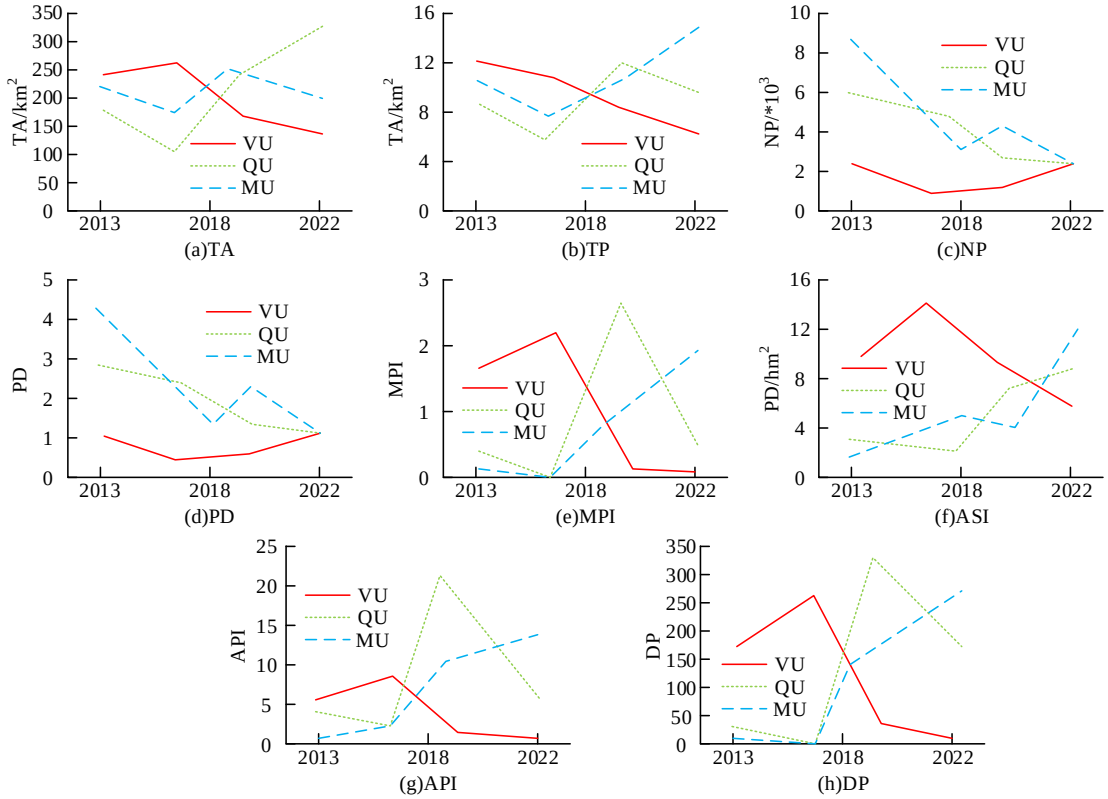

Fig.4 The change of HI landscape index from the perspective of type level from 2013 to 2022

Figure 4 shows the changes in HI landscape index from type level from 2013 to 2022. In Figure 4, the trend of changes in TA and TP is the same, and the changes were relatively stable from 2013 to 2018. VU has a dominant position, with significant fluctuations from 2018 to 2022. The dominant VU has undergone significant changes, transforming into a landscape pattern dominated by MU. There is a significant difference in patch fragmentation among different levels of HIs, and there is a slight increase in NP and PD of VU HIs. MPI and MPA show a rapid downward trend, while API also shows a downward trend. This indicates a transition from a larger area of CU to a lower UHI level. In addition, ASI of VU HI also shows a downward trend. This indicates that the shape of the patches is getting closer to a square, and VU HIs are mostly artificially formed high-temperature areas.

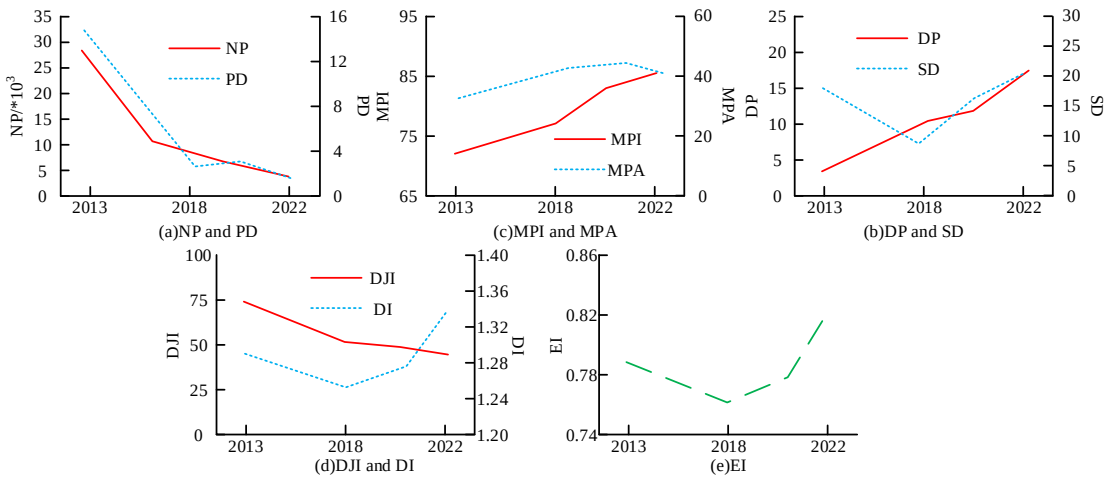

Fig.5 Changes of HI landscape index in landscape level from 2013 to 2022

Figure 5 shows the changes in the HI landscape index from a landscape level perspective from 2013 to 2022. In Figure 5, the NP and PD of the HI show a decreasing trend overall, and the MPA shows an upward trend. This indicates that the rapid development of urbanization has led to a decrease in the fragmentation of HI patches. ASI shows a fluctuating upward trend, and overall it shows a growth trend, with complex shape characteristics. The DP of the study area shows an upward trend, indicating that multiple pixels of the same type aggregate into a patch with closer proximity. The increase in SD in the study area indicates good connectivity and aggregation between different types of plates. DJI showed a slight downward trend, indicating that the type and number of patches around different patches gradually decreased, and the degree of mixed distribution weakened. Both DI and EI showed an upward trend. There is a small difference in the proportion of different types of HI landscape areas in the urbanization development of the research area. However, landscape diversity has increased, and the proportion of different types of HI landscapes is developing towards uniformity.

3.3 Analysis of Urban SP Changes

The time points for RSI collection in the study area, the types of LS series micro, and the threshold for extracting vegetation vary among different years. Therefore, this study is based on this statistical information on changes in vegetation coverage area, water body area and proportion, impermeable surface area and proportion, and the proportion of different temperature zones in the study area.

Table 5 Changes of urban surface vegetation area and water body area in the study area from 2013 to 2022

Time		2013	2018	2022
Vegetation change characteristics	NDVI threshold	0.30	0.30	0.25
	Area /km^2	1108.89	1030.78	840.37
	Average area /km^2	0.0681	0.0635	0.0407
	Patch number	16341	16287	20757
Water change characteristics	MNWBI threshold	0.13	0.15	0.11
	Area /km^2	167.16	159.25	148.12
	Proportion /%	9.60	8.03	7.10

Table 5 shows the changes in urban surface vegetation area and water body area in the study area from 2013 to 2022. In Table 5, from 2013 to 2022, the overall area of vegetation coverage continued to decrease, and the patch number increased. However, the average horizontal area of patches decreased, resulting in a more fragmented vegetation landscape pattern. With greenfield project developing in the later central city, the ecological environment quality and vegetation coverage will be improved. The water area within the study area continues to decrease, with a rate of slowing down from fast to slow. The location with significant changes is at reservoir and lake edge, due to the expansion of the city and the construction of industrial parks.

Table 6 The variation characteristics of urban impervious water surface and surface temperature of different grades in the study area from 2013 to 2022

Time		2013	2018	2022
Change characteristics of impervious water surface	Area /km^2	678.65	787.69	1052.37
	Proportion /%	32.73	37.32	45.58
Characteristics of	Extra high temperature	19.08	19.37	17.48

surface temperature change	zone			
	High-temperature region	8.48	10.54	14.82
	Higher temperature area	14.56	13.58	16.48
	Mesothermal region	18.57	17.66	16.99
	Lower temperature region	25.96	25.51	16.25
	Cryogenic zone	13.42	13.40	18.04

Table 6 shows the variation characteristics of urban impermeable surface and surface temperature at different levels in the study area from 2013 to 2022. In Table 6, the impervious surface area of the study area increased rapidly from 2013 to 2022, reaching 1052.37 km^2 by 2022, accounting for 45.58% of the total area of the study area. Based on the mean and standard deviation results for 2013, 2018, and 2022, it can be divided into six categories: ultra-high, high, relatively high, medium, relatively low, and low temperature zones. From 2013 to 2022, extremely high, high, and relatively high temperature areas that had a significant impact on humans continued to grow.

3.4 Correlation Analysis Between UHI and SP

To further reveal the relationship between UHIE and urban SP through the changes in urban SP in the above-mentioned research area, the distribution of urban SP in 2022 is analyzed by selecting the north-south and east-west direction of the cross-sectional lines.

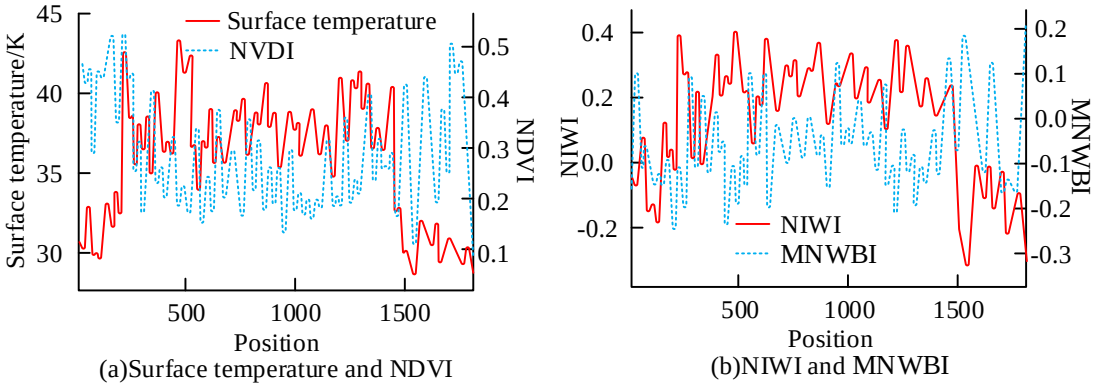

(a)Surface temperature and NDVI (b)NIWI and MNWBI

Fig.6 In 2022, the variation curve of urban surface parameters in the north-south profile of the study area

Figure 6 shows the parameter change curve of the north-south section of the city in the 2022 study area. In Figure 6, on the surface temperature and NIWI profile, the middle region is significantly higher than two ends, while in the NDVI profile, the middle region is significantly lower than the two ends. At around 1500, surface temperature, NVDI, and NIWI are all low values, but in the MNWBI profile, the water body index at this location is significantly higher than other parts.

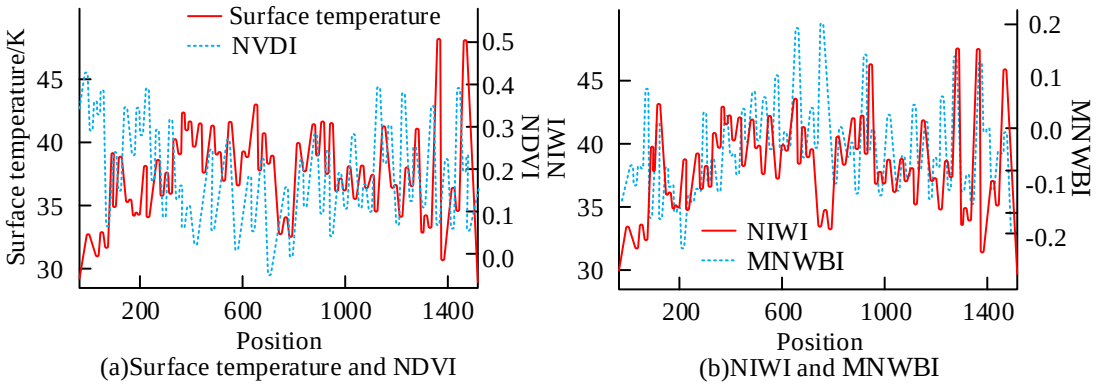

Fig.7 The change curve of urban surface parameters in the east-west section of the study area in 2022

Figure 7 shows the urban SP change curve in the east-west section of the study area in 2022. In Figure 7, the variation curves of surface temperature and NIWI are similar, with low to high distribution from west to east, while the profile changes of NDVI are opposite. The vegetation coverage around the four districts around the city is relatively good. On MNWBI profile, there are differences with changes in water bodies. The above results indicate that surface temperature, NDVI, and NIWI generally radiate from central urban area to the surrounding areas. The surface temperature in the central urban area is higher, while NDVI is lower, and most regional data is not transparent to the water surface. The change trend of surface temperature is opposite to that of NDVI and MNWBI, and consistent with that of NIWI. This shows that surface temperature is negatively correlated with vegetation and water bodies, and positively correlated with impermeable surfaces. To conduct in-depth analysis of surface temperature, vegetation, water bodies, and impermeable surfaces, statistical methods were used for analysis. The software ArcGIS was used for uniform sampling, and the sampling results were then imported into SPSS.

Table 7 Regression equation of land surface temperature and vegetation index and water body index

Tine		2013	2018	2022
Vegetation index	Regression equation	$T_S = -16.802NDVI + 49.073$	$T_S = -13.983NDVI + 41.142$	$T_S = -17.090NDVI + 44.675$
	R^2	0.615	0.632	0.620
Water index	Regression equation	$T_S = -4.425NDVI + 38.352$	$T_S = -4.387NDVI + 33.177$	$T_S = -9.803NDVI + 40.043$
	R^2	0.676	0.740	0.762

Table 7 shows the regression equation between surface temperature, vegetation index, and water body index. In Table 7, surface temperature and vegetation index are correlated negatively, and the best fit equation is a linear function. This indicates that surface temperature will decrease with the increase of NDVI, and vegetation can effectively reduce the surface temperature in the vegetation coverage area and surrounding areas. This also confirms that surface temperature and NDVI are correlated negatively.

Table 8 Statistical results of impervious water surface, vegetation and water body in different HI and green island regions were studied

Time	UHIE	Vegetation water body	Water body	Impervious surface	Sum total

2013	HI	221.13	4.61	650.17	875.84
	Green Island	887.97	195.23	28.52	1111.72
2018	HI	180.16	3.12	693.22	876.5
	Green Island	851.07	156.22	82.43	1089.72
2022	HI	95.38	2.68	907.18	1005.24
	Green Island	745.08	145.42	18.76	909.26

Table 8 shows the statistical results of impermeable water surfaces, vegetation, and water bodies in the HI and green island regions at different times. In Table 8, from 2013 to 2018, the area of the HI area was smaller than that of the green island area. In 2022, the area of the HI continued to grow and surpassed that of the Green Island area, and the impermeable surface of the HI area also showed an increasing trend, from 650.17 km2 in 2013 to 907.18 km2 in 2022. Between 2013 and 2022, over 90% of impermeable surfaces belonged to the HI region. Over 80% of the vegetation belongs to the Green Island area, and over 97% of the water bodies belong to the Green Island area. In summary, the distribution of impermeable surfaces and HI areas remains consistent, while vegetation and water bodies remain consistent with the distribution of green islands.

4 Conclusion

In recent years, with urbanization and infrastructure projects developing rapidly, the land area of cities has been continuously expanding. A large amount of vegetation and water around the city has gradually transformed into artificially made impermeable surfaces, damaging its ecosystem and seriously exacerbating UHIE. To alleviate the impact of UHIE on urban energy use and environmental issues, this study selected Tianjin region with significant UHIE as the research area. The analysis of UHIE from the perspective of urban SP changes provides a scientific basis for UHI prevention and mitigation. Over time, the HI area of the study area increased accordingly, and the proportion of HI area to total area of the study area in 2013, 2018, and 2022 was 41.92%, 48.73%, and 49.16%, respectively. The proportion of VU continues to decrease over time, from 6.95% in 2013 to 3.71%, and RU and MU overall show an increasing trend. The central urban area has become a HI area from 97.92% of the area, and showed a decreasing trend from 2018 to 2022. Among them, VU decreased more significantly, from 55.76% in 2013 to 10.58% in 2022, a decrease of 45.18%. The area of RU and MU increased significantly, from 19.47% in 2013 to 50.90% in 2022, an increase of 31.43%. The corresponding HI area of four districts around the city shows an overall growth trend. In 2013, different regions accounted for 33.64%~41.19% of the total area. Jinnan District has the largest HI area and Xiqing District has the smallest. In 2022, different regions will account for 40.21%~54.22% of the total area. At this time, Dongli District will have the largest HI area and Jinnan District will have the smallest. Overall, surface temperature, NDVI, and NIWI radiate from the central urban area to the surrounding areas. The surface temperature in central urban area is higher, NDVI is lower, and most regional data is not transparent to the water surface. The change trend of surface temperature is opposite to that of NDVI and MNWBI, and consistent with that of NIWI. This indicates that surface temperature is negatively correlated with vegetation and water bodies, and positively correlated with impermeable surfaces. Between 2013 and 2022, over 90% of impermeable water surfaces belonged to the HI area, over 80% of vegetation belonged to the green island area, and over 97% of water bodies belonged to the green island area. In summary, the study scientifically and reasonably analyzed the relationship between UHIE in the study area and urban SP changes,

providing reference for proposing measures to alleviate UHIE. However, there are still shortcomings in the research, which only proposes opinions on governance and link UHI from the perspective of changes in surface parameters. However, it has not been applied in reality, and the generation of UHIE is influenced by multiple factors. In the future, it is necessary to conduct comprehensive analysis from other perspectives and propose practical measures to achieve sustainable development of cities. In addition, building energy consumption is significantly affected by UHIE. The analysis of the impact of UHIE on building heating systems is beneficial for reducing the total energy consumption of social terminals, reducing pollution gas emissions, and promoting China's ecological civilization construction. Therefore, in future research, the mechanism of UHIE on building heating systems can be further explored, providing solid support for government energy-saving decision-making and refined heating services for heating departments.

Reference

[1] A. H. Net, L. C. Durante, I. J. A. Callejas, E. L. A. D. Guarda and J. V. R. Moreia, “The challenges on operating a zero net energy building facing global warming conditions,” Building Simulation, vol. 15, no. 3, pp. 435-451, Jun. 2022. DOI:10.1007/s12273-021-0809-4.

[2] Y. Hu, “From global warming to complex physical systems: Reading of the 2021 Nobel Prize in Physics,” Chinese Science Bulletin, vol. 67, no. 6, pp. 548-556, Apr. 2022. DOI:10.1360/TB-2021-1147.

[3] S. Chen, Y. Yang, F. Deng F, Y. Zhang, D. Liu, C. Liu and Z. Gao, “A high-resolution monitoring approach of canopy urban heat island using a random forest model and multi-platform observations,” Atmospheric Measurement Techniques, vol. 15, no. 3, pp. 735-756, Feb. 2022. DOI:10.5194/amt-15-735-2022.

[4] M. Meftahi, M. Monavari, M. K. Zarkesh, A. Vafaeinejad and A. Jozi, “Achieving sustainable development goals through the study of urban heat island changes and its effective factors using spatio-temporal techniques: The case study (Tehran city),” Blackwell Publishing, vol. 46, no. 1, pp. 88-115, Mar. 2022. DOI: 10.1111/1477-8947.12245.

[5] X. Zhou, Y. Wang, J. Sun, W. Duan, D. Yang, “A Numerical Simulation of Urban Heat Island Effect in Kunming,” Chinese Journal of Atmospheric Sciences, vol. 46, no. 4, pp. 921-935, Nov. 2022. DOI: 10.3878/j.issn.1006-9895.2105.21062.

[6] H. Azarijafari, J.Gregory and R. Kirchain, “Urban-Scale Evaluation of Cool Pavement Impacts on the Urban Heat Island Effect and Climate Change,” Environmental science & technology, vol. 55, no. 17, pp. 11501-11510, Aug. 2021. DOI:10.31224/osf.io/7azwj.

[7] Y. Wang Y, R. Sun, “Impacts of regional climate on urban heat islands in China,” Acta Ecologica Sinica, vol. 41, no. 11, pp. 4288-4299, Jan. 2021. DOI:10.5846/stxb202011303061.

[8] Z. Li, M. Xie, H. Wang, B. Chen, R. Wu and Y. Chen, “The SH of the relationship between PM2.5concentrations and the surface urban heat island effect in Beijing, China:,” Progress in Physical Geography: Earth and Environment, vol. 46, no. 1, pp. 84-104, Aug. 2022. DOI:10.1177/03091333211033209.

[9] C. D. Tranaltes, J. Dunn, J. M. Martin and J. C. Johnson, “Siblicide in the city: the urban heat island accelerates sibling cannibalism in the black widow spider (Latrodectus hesperus),” Urban ecosystems, vol. 25, no. 1, pp. 305-312, Aug. 2022. DOI:10.1007/s11252-021-01148-w

[10] E. Marques, V. Masson, P. Naveau O. Mestre, V. Dubreuil and Y. Richard, “Urban Heat Island Estimation from Crowdsensing Thermometers Embedded in Personal Cars,” Bulletin of the

American Meteorological Society, vol. 103, no. 4, pp. E1098-E1113, Apr. 2022. DOI:10.1175/BAMS-D-21-0174.1
[11] Sengupta R, Fan J Y. Montreal's environmental justice problem with respect to the urban heat island phenomenon. The Canadian Geographer / Le Géographe canadien, vol. 66, no. 2, pp. 307-321, May. 2022. DOI:10.1111/cag.12690.
[12] S. Mamatha, D. Haware, "Document on fluoride accumulation in ground and surface water of Mysore, Karnataka, India," Current World Environment, vol. 8, no. 2, pp. 259-265, Aug. 2021. DOI:10.12944/CWE.8.2.11.
[13] M. A. Alatorre-Zamora, J. O. Campos-Enriquez, E. Fregoso, S. I. SI Belmonte‐Jiménez, R. Chávez‐Segura and M. Gaona‐Mota, "Basement faults deduction at a dumpsite using advanced analysis of gravity and magnetic anomalies," Near Surface Geophysics, vol. 18, no. 3, pp. 307-331, Jan. 2020. DOI:10.1002/nsg.12093.
[14] P. Salinas, A. Bongiorno, I. Romero, C. Veuthey and N. Bruna, "Impact of Maternal Exposure to Wood Smoke Pollution on Fetal Lung Morphology in a Rat Model," International Journal of Morphology, vol. 38, no. 5, pp. 1250-1257, Oct. 2020. DOI:10.4067/S0717-95022020000501250.
[15] G. Duan, T. Takemi, "Predicting urban surface roughness aerodynamic parameters using random forest," Journal of Applied Meteorology and Climatology, vol. 60, no. 7, pp. 999-1018, Jul. 2021. DOI:10.1175/JAMC-D-20-0266.1.
[16] Y. Hou, C. Liu, X. U. Zhongbo, A. N. Yuhua and L. I. Jingling, "A Method for Rapidly Predicting Recovery of Multi-Layer Oilfields Developed by Water-Flooding," Petroleum Drilling Techniques, vol. 50, no. 5, pp. 82-87, Oct. 2022. DOI:10.11911/syztjs.2022102.
[17] C. Yang, F. Yang, C. Ding, "Linking leader humor to employee creativity: the roles of relational energy and traditionality," Journal of Managerial Psychology, vol. 36, no. 7, pp. 548-561, Apr. 2021. DOI:10.1108/JMP-06-2020-0300.
[18] Z. We, L. Duo, L. B. Zhi, Y. Y. Jin, "Construction and Optimization of p-coumaric Acid Producing Saccharomyces cerevisiae," Chinese Journal of Biotechnology, vol. 36, no. 9, pp. 1838-1848, Sep. 2020. DOI: 10.13345/j.cjb.200003.
[19] Z. Wu, Y. Zhao, N. Zhang, "A Literature Survey of Green and Low-Carbon Economics Using Natural Experiment Approaches in Top Field Journal," Green and Low-Carbon Economy, vol. 1, no. 1, pp. 2-14, Mar. 2023. DOI:10.47852/bonviewGLCE3202827.
[20] A. M. Usman, M. K. Abdullah, "An Assessment of Building Energy Consumption Characteristics Using Analytical Energy and Carbon Footprint Assessment Model," Green and Low-Carbon Economy, 2023, 1(1): 28-40.vol. 1, no. 1, pp. 28-40, Mar. 2023. DOI:10.47852/bonviewGLCE3202545

Submitted: 05.12.2023.
Revised: 18.02.2024.
Accepted: 19.03.2024.